Article

Sub-Nanosecond Passively Q-Switched Yellow and Orange Raman Lasers

Yu-Wen Ho [1], Jian-Cheng Chen [1], Yueh-Chi Tu [1], Hsing-Chih Liang [2] and Yung-Fu Chen [1,*]

[1] Department of Electrophysics, National Yang Ming Chiao Tung University, Hsinchu 30010, Taiwan; wayneho4415.sc11@nycu.edu.tw (Y.-W.H.); rf0010505.sc10@nycu.edu.tw (J.-C.C.); doochy928.sc09@nycu.edu.tw (Y.-C.T.)

[2] Institute of Physics, National Yang Ming Chiao Tung University, Hsinchu 30010, Taiwan; hcliang@nycu.edu.tw

* Correspondence: yfchen@nycu.edu.tw

Abstract: Sub-nanosecond high-peak-power passively Q-switched yellow and orange lasers are compactly developed using a near-concentric resonator with intracavity-stimulated Raman scattering (SRS) as well as second harmonic generation (SHG). The fundamental wave is generated from an *a*-cut Nd:YVO$_4$ crystal. The Stokes wave for an SHG yellow (579 nm) or orange (589 nm) laser is generated from a Np-cut potassium gadolinium tungstate (KGW) with the N_g or N_m axis parallel to the *c*-axis of Nd:YVO$_4$ crystal. The optimal cavity length is systematically explored in a near-concentric configuration to achieve sub-nanosecond high-peak-power pulses. The shortest pulse widths for the yellow and orange output pulses are down to 0.67 ns and 0.70 ns, respectively. The highest peak powers for the yellow and orange output pulses are up to 176 and 138 kW, respectively.

Keywords: stimulated Raman scattering; passively Q-switched laser; Nd:YVO$_4$ crystal; KGW crystal

1. Introduction

Sub-nanosecond passively Q-switched laser pulses with high peak power (>10 kW) are greatly appropriate for many applications including nonlinear wavelength, high-precision measurements, laser-induced plasma ignition, and free-space communications [1–4]. High-peak-power pulsed lasers with wavelengths between 550 and 600 nanometers (nm) are particularly useful in biomedical applications such as dermatology [5], ophthalmology [6], biological analysis [7], flow cytometry [8], and photoacoustic microscopy [9]. Yellow pulsed lasers with wavelengths between 572 and 582 nm can be well absorbed by oxygenated hemoglobin. As a result, yellow lasers have been widely adopted in medical treatments [10,11]. Furthermore, high-peak-power orange lasers near 589 nm are almost indispensable in the applications of atmospheric lidar [12] and sodium guide stars [13,14]. So far, the technologies for developing yellow–orange lasers consist of solid-state lasers [15,16], fiber lasers [17], semiconductor lasers [18], and optically pumped semiconductor lasers [19]. Among these technologies, solid-state lasers are especially prospective for generating high-peak-power pulses due to their long lifetime of the upper-level state and the flexible combination with nonlinear optics.

The method for generating high-power Nd-doped crystal lasers in the yellow–orange region usually comprises two stages of intracavity nonlinear wavelength conversions, which are stimulated Raman scattering (SRS) and second harmonic generation (SHG). Raman scattering is a process of inelastic scattering in which incident photons interact with molecules, gaining or losing energy, leading to a change in the frequency of scattered photons. The growing applications in various fields create a great demand for developing reliable all-solid-state lasers in previously uncovered spectral regions. In comparison with gaseous and liquid Raman cells, the advantages of SRS in solid-state crystals include higher conversion efficiency, no need for phase matching, and easier handling. The potassium

gadolinium tungstate KGd(WO$_4$)$_2$ or KGW single crystal has been confirmed to be a very promising Raman material due to its low structure symmetry and high χ^3-nonlinearity. Furthermore, the KGW crystal possesses a powerful Raman spectrum extending from ultraviolet to near-infrared, so it can be used as a reference material for the Raman spectrum as well as samples to study solid Raman scattering.

Not only the continuous-wave and quasi-continuous-wave operation [20–22] but also the actively and passively Q-switched yellow–orange lasers have been widely investigated [23,24]. Compared with active Q-switched operation, passive Q-switched solid-state lasers have the advantages of compactness, simplicity, and robustness [25,26]. Furthermore, the timing jitter due to the fluctuation in the pump and emission is the common critical issue of passively Q-switched lasers [27], which has been substantially improved with pulse pumping using a shorter pump duration and a higher pump power [28,29]. As a consequence, passively Q-switched lasers can be greatly applicable to various fields, such as micromachining, medical treatment, lidar, and ranging. Nevertheless, sub-nanosecond high-peak-power Q-switched yellow and orange lasers have never been demonstrated so far.

Previously, we used a near-concentric cavity to realize an efficient passively Q-switched Nd:YVO$_4$ Raman laser at 589 nm with a KGW as an intracavity Raman gain medium at the shift of 901 cm^{-1} [23]. For achieving a passive Q-switching efficiency [30], we employed a near-concentric resonator to generate a large value of α via the beam focusing on the saturable absorber. The parameter α can be given by $\alpha = A\sigma_{gs}/(\gamma A_s \sigma)$, where A and A_s are the mode areas for the fundamental wave in the gain medium and saturable absorber, respectively; σ_{gs} and σ are the cross sections for the ground-state absorption of the saturable absorber and the stimulated emission of the gain medium, respectively; and γ is the inversion reduction factor. Furthermore, the near-concentric resonator is combined with an internal cavity to yield the SRS and SHG. In this exploration, we extend this approach to achieve sub-nanosecond high-peak-power passively Q-switched yellow and orange lasers with intracavity SRS and SHG processes. By using the KGW Raman gain medium, the Stokes emissions for generating yellow (579 nm) and orange (589 nm) lasers using SHG can be selectively accomplished by orienting the KGW crystal. We use lithium triborate crystals, known as LBO (LiB$_3$O$_5$), to perform the intracavity SHG. The LBO crystal, belonging to an orthorhombic system with a point group symmetry of mm^2, is a negative biaxial crystal that is very promising in the fabrication of nonlinear optical components such as harmonic generators and optical parametric oscillators due to its excellent nonlinear optical properties [31]. Compared with lithium niobate (LiNbO$_3$), one of the most widely used nonlinear optical crystals in photonic applications [32,33], LBO has a higher damage threshold (~10 GW/cm^2), thus being applied to operations with ultra-high intensity regimes. In addition, compared with many other nonlinear optical crystals (such as DKDP and YCOB), LBO also has broadband transparency from 160 to 2600 nm, a larger temperature and angle acceptance bandwidth, and a higher nonlinear optical frequency conversion efficiency. The LBO-based SHG process was first demonstrated by Chen et al. in 1989 [31]. One year later, Zhao et al. realized high-efficiency SHG based on LBO with a conversion efficiency of 60% at a 1064 nm wavelength [34]. By 2021, the efficiency had increased to approximately 80% with a light intensity of 10$^{18–19}$ W/cm^2 [35], demonstrating LBO's great potential in high energy density applications. In this work, the optimal cavity length is systematically explored to generate a sub-nanosecond pulse duration to surpass previous works [14–16,23]. Under the optimal circumstance, the highest pulse energy and shortest pulse width for the yellow output are found to be 118 µJ and 0.67 ns, respectively. On the other hand, the highest pulse energy and shortest pulse width are 97 µJ and 0.70 ns for the orange output. The peak powers for the yellow and orange outputs are up to approximately 176 and 138 kW, respectively. In previous results, the obtained peak powers for yellow–orange lasers were approximately 81.4 W [14], 16 kW [15], and 118 kW [23]. To the best of our knowledge, these peak powers are the highest values obtained in sub-nanosecond passively Q-switched yellow and orange lasers.

2. Theoretical Model and Experimental Setup

Since passively Q-switched lasers eliminate a potential hazard of failure in high-voltage switching electronics of actively Q-switched lasers, the NASA space systems employed passive Q-switching technology instead of active Q-switching to increase reliability. Recently, we developed a pedagogically fast model for accurately analyzing PQS lasers in a full scope of output coupling [30]. We considered the spatial overlap effect in deriving the characteristic equation for the photon density from the coupled rate equations for the four-level PQS laser. The derived transcendental equation can be numerically solved to obtain an analytical form for the residual fraction of the inversion density after the Q-switched pulse is complete. The developed model and equations were systematically validated with experimental explorations. The rate equations were used to analyze the operation of a four-level passively Q-switched laser [30]. From the analyzed result, the output efficiency can be characterized by the transcendental equation

$$\xi(1 - \mu) - [(\xi - 1)(1 - \mu^{\alpha})/\alpha] - \ln(1/\mu) = 0, \tag{1}$$

where $\xi = N_i/N_t$, $\mu = N_f/N_i$, N_i is the initial inversion population for reaching the pulse generation, N_t is the transition population relevant to the pulse peak, and N_f is the final population when the pulse ends. In the limit of $\alpha \to \infty$, Equation (1) can be simplified as $\xi(1 - \mu) - \ln(1/\mu) = 0$, which is the characteristic equation for an ideal active Q-switching. It can be numerically confirmed that the larger the value of the parameter α is, the higher the output efficiency becomes [30]. Even so, the output efficiency obviously tends to saturate for $\alpha > 5$. Figure 1 depicts the setup of the laser resonator. A fiber-coupled semiconductor laser with a central wavelength of 808 nm was used as the pump source. The specification of the coupled fiber was 200 μm for the core diameter and 0.22 for the numerical aperture. The maximum instantaneous pump power could be up to 40 W. To reduce the timing jitter, the pump source was precisely modulated with a square duration of 40 μs at a fixed frequency of 10 kHz. The laser material was an *a*-cut 0.2 at.% Nd:YVO$_4$ crystal with the dimension of $3 \times 3 \times 20$ mm^3. The coatings on both end surfaces of the laser crystal were anti-reflective (AR) at 808 and 1064 nm (reflectance < 0.2%). The Nd:YVO$_4$ crystal was placed close to the input mirror at a distance of 1.0 mm. Both the input mirror and the output coupler were plano-concave mirrors with the same radius of curvature of 50 mm. The radius of curvature was chosen to allow the cavity length to be as short as possible, which is the critical factor for generating a sub-nanosecond pulse width. The coating on the plano side of the input mirror was AR at 808 nm (reflectance < 0.2%). The coating on the concave side of the input mirror was highly reflective (HR) in the region of 1000 to 1200 nm (reflectance > 99.9%) and highly transmissive (HT) at 808 nm (transmittance > 95%). The coating on the concave side of the output coupler was HR at 1050–1180 nm (reflectance > 99.9%) and HT at 570–590 nm (transmittance > 95%). The coating on the plano side of the output coupler was AR at 570–590 nm (reflectance < 0.2%).

The saturable absorber was a Cr^{4+}:YAG crystal with the initial transmission of $T_o = 50\%$ and the dimension of $3 \times 3 \times 2$ mm^3. The coatings on both sides of the saturable absorber were AR in the range of 1060 to 1180 nm (reflectance < 0.2%). The saturable absorber was located near the center of the resonator. The Raman gain material for the intracavity SRS was a Np-cut KGW crystal with the dimension of $3 \times 3 \times 20$ mm^3. The spontaneous Raman spectrum of the KGW crystal [25,26] revealed that the highest Raman shifts were 768 and 901 cm^{-1} for the polarization of the excited wave to be along the N_g and N_m axes, respectively. As a consequence, the 579 nm yellow and 589 nm orange outputs could be individually generated by setting the *c*-axis of the Nd:YVO$_4$ crystal to be along the N_g and N_m axes, respectively. Note that the polarization of the fundamental wave was usually along the c-axis of the Nd:YVO$_4$ crystal. The coating on the first side of the KGW crystal toward the input mirror was HR at 1150–1180 nm (reflectance > 99.9%) and HT at 1064 nm (transmittance > 99%). The second side of the KGW crystal toward the output coupler was coated to be HT (transmittance > 99%) for 1064 nm and 1150–1180 nm and

HR for 570–590 nm (reflectance > 99%) to avoid the backward yellow–orange generation being absorbed by the Nd:YVO$_4$ crystal. The Nd:YVO$_4$, Cr^{4+}:YAG, and KGW crystals were enclosed with indium foils and were packaged in copper holders with active cooling at 20 °C. The intracavity frequency doubling of the Stokes wave was generated by using an LBO with the cut angles of $\theta = 90°$ and $\phi = 3.9°$. The dimension of the LBO crystal was $3 \times 3 \times 8$ mm^3. The coatings on both sides of the LBO crystal were AR at the wavelengths covering 570–590, 1064, and 1150–1180 nm (reflectance < 0.2%). The LBO crystal was placed into a copper holder. The temperature of the LBO crystal was precisely controlled to achieve the critical phase matching. The separations among the Cr^{4+}:YAG, KGW, and LBO crystals were all within 1.0 mm. The emission wavelength spectra were measured with an optical spectrum analyzer with a resolution of 0.1 nm (Advantest Q8381A, Japan). A high-speed GaAs photodetector (Electro-optics Technology Inc. ET-4000, rise time 30 ps, Warwick, UK) was used to measure the temporal properties of the Q-switched laser, and a digital oscilloscope (Teledyne LeCroy, Wave Master 820Zi-A, Ramapo, NY, USA) was used to record its output signal.
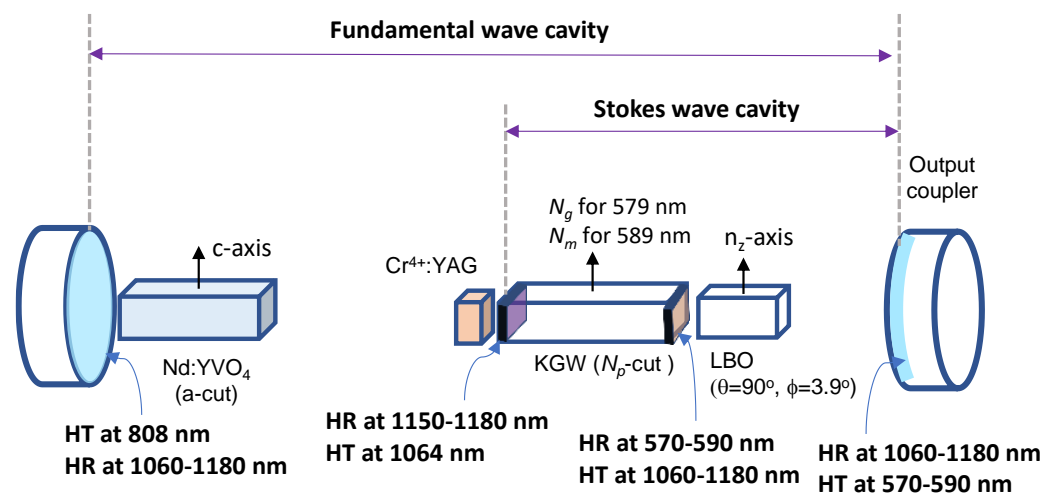

Figure 1. Cavity setup for generating sub-nanosecond passively Q-switched Nd:YVO$_4$/KGW yellow and orange lasers with intracavity SHG.

3. Cavity Design

From the cavity configuration depicted in Figure 1, the optical length L_{cav}^* of the laser resonator can be expressed as

$$L_{cav}^* = L_{cav} - \sum_{j=1}^{4} \left(1 - \frac{1}{n_j} \right) \updownarrow_j, \tag{2}$$

where L_{cav} represents the geometric length of the cavity for the fundamental wave; $\updownarrow_1$, $\updownarrow_2$, $\updownarrow_3$, and $\updownarrow_4$ are the lengths of the Nd:YVO$_4$, Cr^{4+}:YAG, KGW, and LBO crystals, respectively; and n_1, n_2, n_3, and n_4 are the refractive indices of their counterparts. The transverse modes can then be obtained from the ABCD matrix components for one complete round trip in a resonator. Since the Nd:YVO$_4$ crystal was placed quite close to the input mirror, the mode size in the laser gain medium can be reasonably computed with the cavity mode radius on the input mirror, which is given by

$$\omega_c = \left[\frac{\lambda R}{\pi} \sqrt{\frac{L_{cav}^*}{(2R - L_{cav}^*)}} \right]^{1/2}, \tag{3}$$

where R is the radius of curvature of the cavity mirrors and λ is the wavelength of the fundamental wave. On the other hand, the Cr^{4+}:YAG crystal was placed near the beam

waist of the laser cavity. Accordingly, the mode size in the saturable absorber can be computed with the cavity mode radius at the beam waist, which is given by

$$\omega_s = \left[\frac{\lambda}{2\pi} \sqrt{L_{cav}^*(2R - L_{cav}^*)} \right]^{1/2}, \tag{4}$$

From Equations (3) and (4), the mode area ratio can be simplified as $A/A_s = 2R/(2R - L_{cav}^*)$. With the values of σ and σ_{gs}, the parameter $\alpha = A\sigma_{gs}/(A_s\sigma)$ can be conveniently calculated as a function of L_{cav}^*. Figure 2 shows the calculated results for the parameter α as a function of L_{cav}^* in the region near the concentric configuration. Note that the cavity length L_{cav}^* for the concentric configuration is 100 mm. The value of the parameter α can be seen to increase significantly from 5 to 20 with increasing the cavity length from 88 to 97 mm. In the following, experimental results for exploring the dependence of the output performance on the cavity length near the concentric cavity are systematically presented.
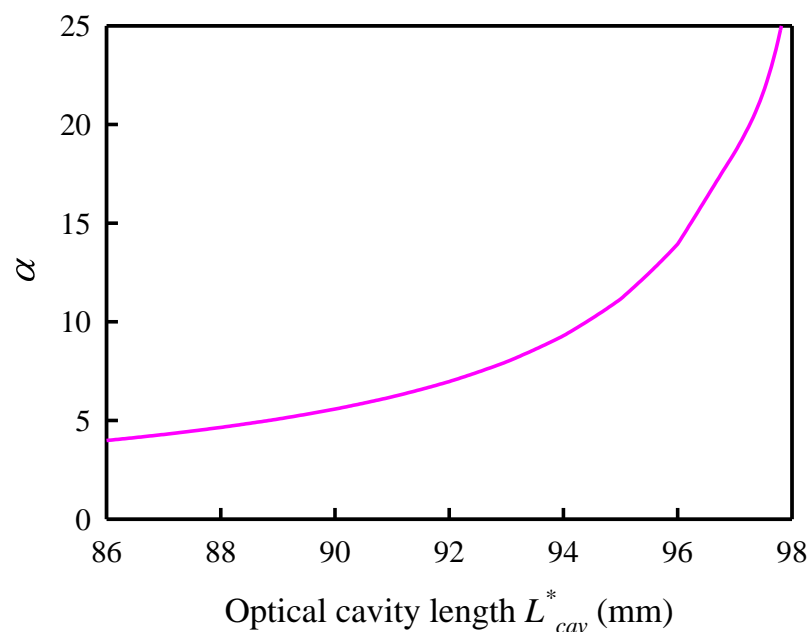

Figure 2. Calculated results for the parameter α as a function of L_{cav}^* in the region near the concentric configuration.

4. Analysis of Second Harmonic Generation

We used an LBO crystal with the type-I phase matching angle in the XY plane to achieve an SHG of 1159 nm for the yellow output and an SHG of 1176 nm for the orange output. The unit cell dimension of LBO is given by a = 8.4473 Å, b = 7.3788 Å, and c = 5.1395 Å. The principal axes X, Y, and Z ($n_z > n_y > n_x$) of the LBO crystal are parallel to the crystallographic axes a, c, and b, respectively. The temperature-dependent Sellmeier equations of n_x, n_y, and n_z for the LBO crystal can be given by [36]

$$n_x(\lambda, T) = \left(2.4542 + \frac{0.01125}{\lambda^2 - 0.01135} - 0.01388\lambda^2 \right)^{1/2} + \frac{dn_x}{dT}(T - T_o), \tag{5}$$

$$n_y(\lambda, T) = \left(2.5390 + \frac{0.01277}{\lambda^2 - 0.01189} - 0.01848\lambda^2 \right)^{1/2} + \frac{dn_y}{dT}(T - T_o), \tag{6}$$

$$n_z(\lambda, T) = \left(2.5865 + \frac{0.01310}{\lambda^2 - 0.01223} - 0.01861\lambda^2 \right)^{1/2} + \frac{dn_z}{dT}(T - T_o), \tag{7}$$

where the units of wavelength λ are micrometers, the units of temperature T are degrees Celsius, and $T_o = 20\ °C$. From the work by Velsko et al. [37], the three thermo-optical coefficients are given by

$$\frac{dn_x}{dT} = -1.8 \times 10^{-6}, \tag{8}$$

$$\frac{dn_y}{dT} = -13.6 \times 10^{-6}, \tag{9}$$

$$\frac{dn_z}{dT} = -(6.3 + 2.1\lambda) \times 10^{-6}. \tag{10}$$

From the work by Tang et al. [38], the three thermo-optical coefficients are given by

$$\frac{dn_x}{dT} = 2.0342 \times 10^{-7} - 1.9697 \times 10^{-8}T - 1.4415 \times 10^{-11}T^2, \tag{11}$$

$$\frac{dn_y}{dT} = -1.0748 \times 10^{-5} - 7.1034 \times 10^{-8}T - 5.7387 \times 10^{-11}T^2, \tag{12}$$

$$\frac{dn_z}{dT} = -8.5998 \times 10^{-7} - 1.5476 \times 10^{-7}T + 9.4675 \times 10^{-10}T^2 - 2.2375 \times 10^{-12}T^3. \tag{13}$$

The type-I phase matching in the XY plane of the LBO crystal is similar to that in the negative uniaxial crystal. The phase-matching condition for the SHG of the wavelength λ can be expressed as

$$n_z(\lambda, T) = n_{xy}^e(\lambda/2, T, \phi). \tag{14}$$

The effective refractive index $n_{xy}^e(\lambda/2, T, \phi)$ is given by

$$n_{xy}^e(\lambda/2, T, \phi) = \left[\frac{\sin^2 \phi}{n_x^2(\lambda/2, T)} + \frac{\cos^2 \phi}{n_y^2(\lambda/2, T)} \right]^{-1/2}. \tag{15}$$

We used Equations (5)–(15) to calculate the relationship between the phase-matching temperature and the SHG wavelength for the LBO crystal with $\theta = 90°$ and $\phi = 3.9°$. Figure 3 shows the calculated results. It can be seen that the phase-matching temperatures calculated with the model by Tang et al. are generally lower than those calculated with the model by Velsko et al. From the experimental results, the phase-matching temperatures for SHG wavelengths of 589 nm and 579 nm were found to be approximately 24 °C and 34 °C, respectively. The values obtained with the model by Tang et al. were found to be more consistent with the experimental results.
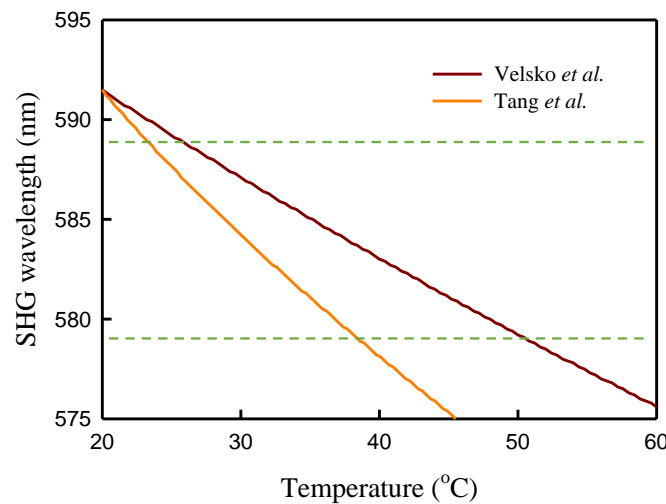

Figure 3. Calculated results for the relationship between the phase-matching temperature and the SHG wavelength for the LBO crystal with $\theta = 90°$ and $\phi = 3.9°$ [37,38].

5. Results and Discussion

　　　Under the condition of pulse pumping, the timing jitter was experimentally found to be in the range of ± 3 μs. The experimental results revealed that there was a threshold pump power at which the output pulse rate could catch up with the pump rate of 10 kHz. From the threshold pump power, the threshold pump energy can be experimentally determined. Figure 4 illustrates the experimental results for the threshold pump energy at 808 nm versus the cavity length L_{cav}^* for the output pulse rate up to 10 kHz. On the whole, the threshold pump energy for the yellow output at 579 nm is approximately 10% higher than that for the orange output at 589 nm for the cavity length L_{cav}^* in the range of 90 and 96 mm. The reason why the threshold pump energy for generating the 579 nm output is higher than that for 589 nm is mainly because of the smaller gain in the Raman shift at 768 cm^{-1} than that at 901 cm^{-1}. Furthermore, it can be seen that the dependence of the threshold pump energy on the cavity length L_{cav}^* is rather insignificant for the scheme of the near-concentric cavity. Even so, the output pulse energy considerably depends on the cavity length L_{cav}^*, as shown in Figure 5. The pulse energy of the yellow output at 579 nm can be seen to increase from 70 to 118 μJ as the cavity length L_{cav}^* increases from 87 to 96 mm. On the other hand, the pulse energy of the orange output at 589 nm increases from 63 to 97 μJ as the cavity length L_{cav}^* increases from 87 to 96 mm. Although the threshold pump energies for the yellow emission are higher than those for the orange output, the higher output energies can be generated for revenues. It is worthwhile to mention that the Cr^{4+}:YAG crystal probably will be damaged for a cavity length within 98 and 100 mm. Therefore, the optimal cavity length should be controlled in the range of 96 ± 1 mm.
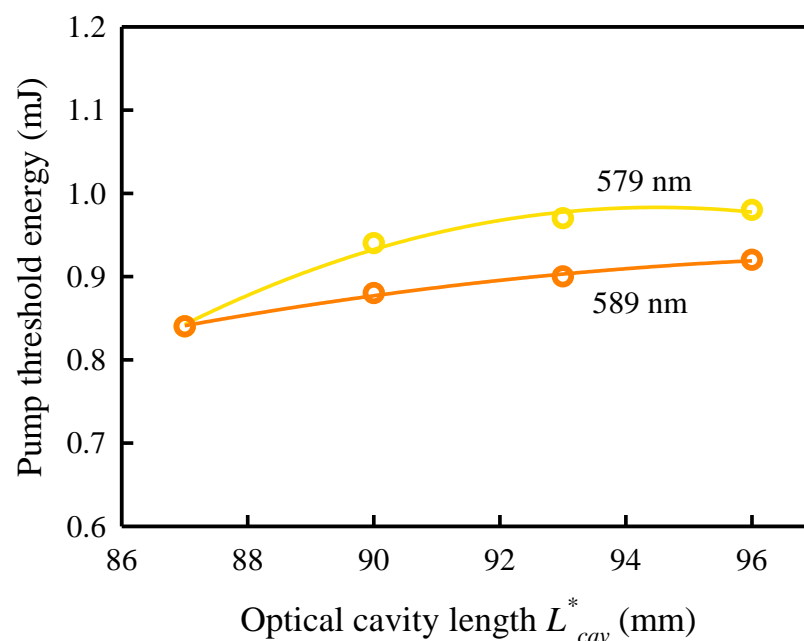

Figure 4. Experimental results for the threshold pump energy at 808 nm versus the cavity length L_{cav}^* for the output pulse rate up to 10 kHz.

　　　Under the circumstance of pulse pumping, the average output power versus the average pump power can be seen to display the characteristics of the staircase due to the mechanism of passive Q-switching. Figure 6 shows the experimental results for the average power of the yellow output at 579 nm versus the average power of the diode input at 808 nm. Several plateaus can be clearly seen in the input–output. Each plateau before the final one displays an output pulse rate corresponding to a fraction of the pump rate, as indicated in Figure 6. The final plateau shown in Figure 6 represents the output rate required to catch up with the pump rate of 10 kHz. A similar input–output feature can be obtained for the orange output, as shown in Figure 7.
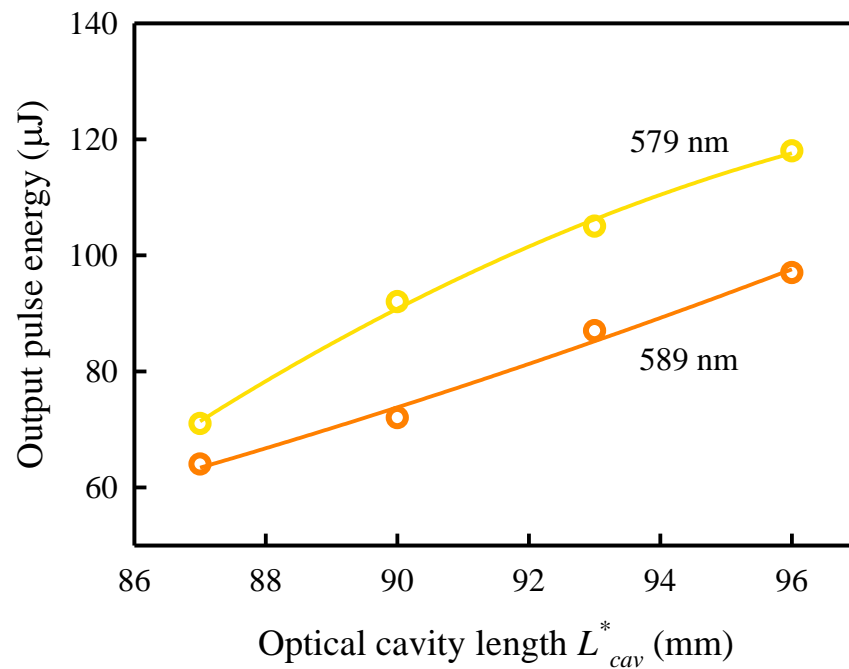
Figure 5. Experimental results for the output pulse energies of yellow and orange lasers versus the cavity length L^*_{cav}.
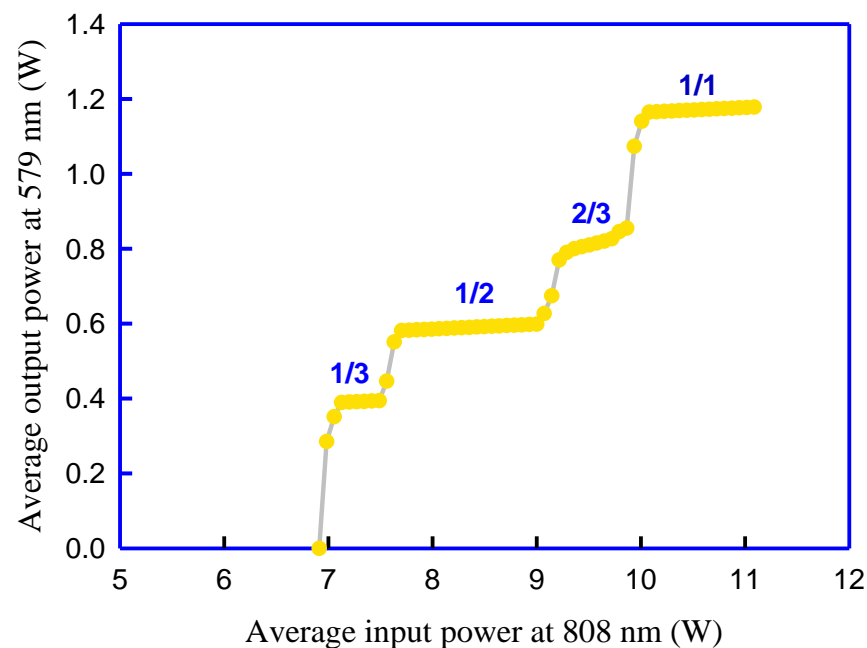

Figure 6. Experimental results for the average power of the yellow output at 579 nm versus the average power of the diode input at 808 nm.

Figure 8 depicts the experimental data for the temporal duration of the output pulses at 579 and 589 nm versus the cavity length L^*_{cav}. It can be seen that the pulse widths for both outputs significantly decrease with an increase in the cavity length L^*_{cav} within 87–93 mm and then approach approximately 0.70 ns in the range of 96 ± 1 mm. The effect of the pulse shortening is mainly due to intracavity-stimulated Raman scattering and efficient passive Q-switching. In addition to the beam waist in the saturable absorber, since the KGW crystal is also very close to the beam waist, the higher output power with increasing cavity length is simultaneously attributed to the smaller beam waist in the KGW crystal leading to a much higher gain. Figure 9a,b shows the typical pulse trains obtained with

the cavity length $L^*_{cav} = 96$ mm for the yellow and orange outputs, respectively. The peak-to-peak fluctuations for the yellow and orange outputs are found to be nearly the same as $\pm 10.0\%$. The temporal profiles are shown in Figure 9c,d for the yellow and orange outputs, respectively. It was confirmed that there were no satellite pulses in either the yellow or orange outputs. From the output pulse energy and pulse duration, the maximal output peak powers for the yellow and orange outputs were calculated to be approximately 176 and 138 kW, respectively. Furthermore, the beam quality M^2 factor was measured from the beam diameter and divergence angle. The measured M^2 factors for both the yellow and orange outputs were found to be approximately 1.5–2.0.
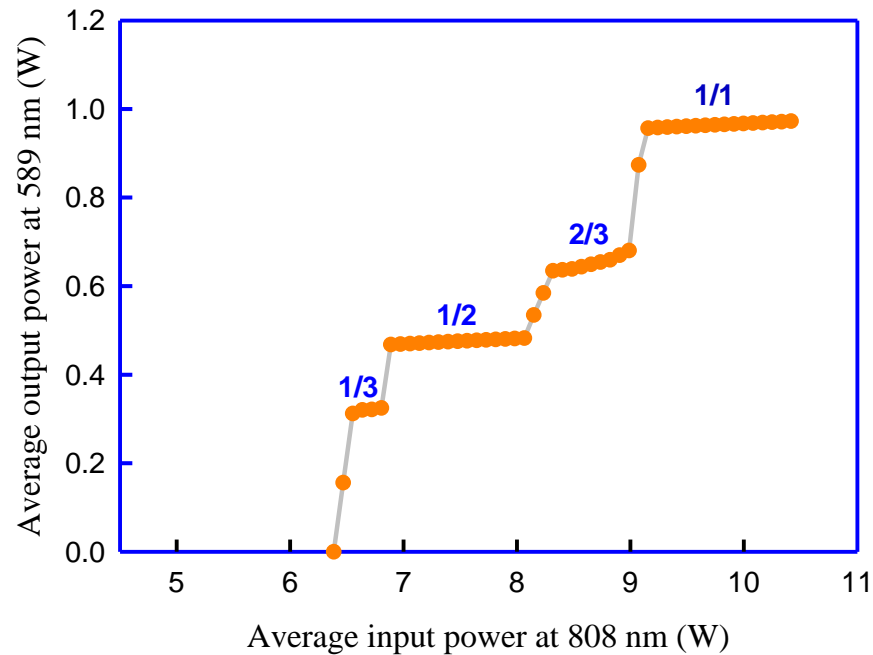

Figure 7. Experimental results for the average power of the yellow output at 589 nm versus the average power of the diode input at 808 nm.
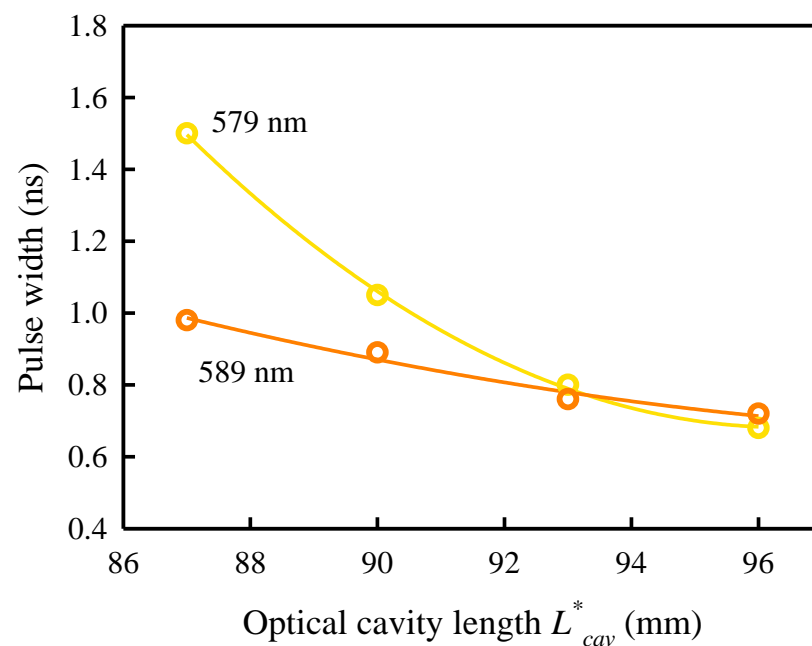

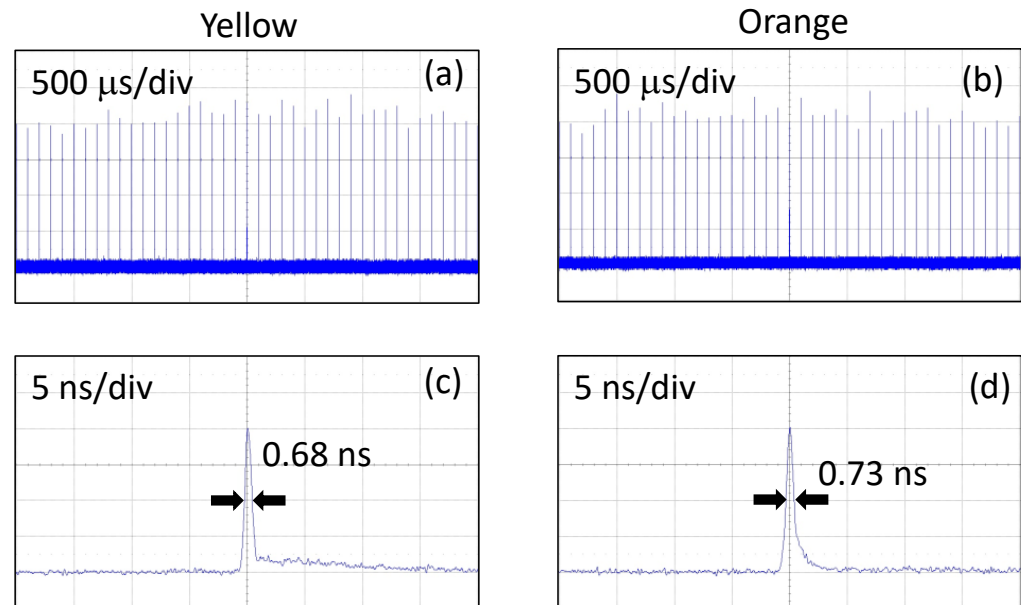**Figure 8.** Experimental data for the temporal duration of the output pulses at 579 and 589 nm versus the cavity length L^*_{cav}.

Figure 9. (**a**,**b**): Typical pulse trains obtained with the cavity length L^*_{cav} mm for the yellow and orange outputs, respectively, and (**c**,**d**) the temporal profiles for the yellow and orange outputs, respectively.

6. Conclusions

In summary, we have demonstrated sub-nanosecond high-peak-power passively Q-switched Nd:YVO$_4$ yellow and orange lasers. We have used an N_p-cut KGW as the Raman gain medium to generate the Stokes wave for the yellow or orange SHG by orienting its N_g or N_m axis to be parallel to the polarization of the fundamental wave. We have systematically explored the optimal cavity length in a near-concentric cavity to achieve sub-nanosecond pulse duration. Under the circumstance of the optimal cavity length, the shortest pulse width for both yellow and orange emissions can be down to less than 0.70 ns. The maximum peak powers for both yellow and orange outputs can be up to greater than 130 kW. To the best of our knowledge, these peak powers are the highest values obtained in sub-nanosecond passively Q-switched yellow and orange lasers.

Author Contributions: Conceptualization, Y.-W.H. and Y.-F.C.; validation, Y.-W.H. and H.-C.L.; formal analysis, J.-C.C. and Y.-F.C.; resources, Y.-C.T. and Y.-F.C.; writing—original draft preparation, Y.-F.C.; writing—review and editing, Y.-W.H., H.-C.L. and Y.-F.C.; supervision, Y.-F.C. All authors have read and agreed to the published version of the manuscript.

Institutional Review Board Statement: Not applicable.

Informed Consent Statement: Not applicable.

Data Availability Statement: Data are contained within the article.

Conflicts of Interest: The authors declare no conflicts of interest.

References

1. Zayhowski, J.J. Passively Q-switched Nd:YAG microchip lasers and applications. *J. Alloys Compd.* **2000**, *303–304*, 393–400. [CrossRef]
2. Swatantran, A.; Tang, H.; Barrett, T.; Decola, P.; Dubayah, R. Rapid, high-resolution forest structure and terrain mapping over large areas using single photon lidar. *Sci. Rep.* **2016**, *6*, 28277. [CrossRef]
3. Eisaman, M.D.; Fan, J.; Migdall, A.; Polyakov, S.V. Invited Review Article: Single-photon sources and detectors. *Rev. Sci. Instrum.* **2011**, *82*, 071101. [CrossRef] [PubMed]
4. Tsunekane, M.; Inohara, T.; Ando, A.; Kido, N.; Kanehara, K.; Taira, T. High Peak Power, Passively Q-switched Microlaser for Ignition of Engines. *IEEE J. Quantum Electron.* **2010**, *46*, 277–284. [CrossRef]

5. Wanner, M.; Sakamoto, F.H.; Avram, M.M.; Chan, H.H.; Alam, M.; Tannous, Z.; Anderson, R.R. Immediate skin responses to laser and light treatments: Therapeutic endpoints: How to obtain efficacy. *J. Am. Acad. Dermatol.* **2016**, *74*, 821–833. [CrossRef] [PubMed]

6. Maia, A.M.; Penha, F.M.; Regatieri, C.V.S.; Cardillo, J.A.; Farah, M.E. Micropulse 577nm-yellow laser photocoagulation for central serous chorio-retinopathy. *Investig. Ophthalmol. Vis. Sci.* **2010**, *51*, 4273.

7. Runcorn, T.H.; Görlitz, F.G.; Murray, R.T.; Kelleher, E.J.R. Visible Raman-shifted Fiber Lasers for Biophotonic Applications. *IEEE J. Sel. Top. Quant. Electron.* **2018**, *24*, 1400208. [CrossRef]

8. Kapoor, V.; Karpov, V.; Linton, C.F.; Subach, V.; Verkhusha, V.V.; Telford, W.G. Solid state yellow and orange lasers for flow cytometry. *Cytom. Part A* **2008**, *73*, 570–577. [CrossRef] [PubMed]

9. Maslov, K.; Zhang, H.F.; Hu, S.; Wang, L.V. Optical-resolution photoacoustic microscopy for in vivo imaging of single capillaries. *Opt. Lett.* **2008**, *33*, 929. [CrossRef]

10. Sadick, N.S.; Weiss, R. The utilization of a new yellow light laser (578 nm) for the treatment of class I red telangiectasia of the lower extremities. *Dermatol. Surg.* **2002**, *28*, 21–25.

11. Lee, H.I. Clinicopathologic efficacy of copper bromide plus/yellow laser (578 nm with 511 nm) for treatment of melasma in Asian patients. *Dermatol. Surg.* **2010**, *36*, 885–893. [CrossRef] [PubMed]

12. Ernstberger, B.; Enderlein, M.; Friedenauer, A.; Schwerdt, R.; Wei, D.; Karpov, V.; Leisching, P.; Clements, W.R.L.; Kaenders, W.G. Robust remote-pumping sodium laser for advanced LIDAR and guide star applications. In *Optics in Atmospheric Propagation and Adaptive Systems XVIII*; SPIE: Bellingham, WA, USA, 2015; Volume 9641.

13. Huo, X.; Qi, Y.; Zhang, Y.; Chen, B.; Bai, Z.; Ding, J.; Wang, Y.; Lu, Z. Research development of 589 nm laser for sodium laser guide stars. *Opt. Lasers Eng.* **2020**, *134*, 106207. [CrossRef]

14. Yang, X.; Zhang, L.; Cui, S.; Fan, T.; Dong, J.; Feng, Y. Sodium guide star laser pulsed at Larmor frequency. *Opt. Lett.* **2017**, *42*, 4351–4354. [CrossRef] [PubMed]

15. Zhang, L.; Duan, Y.; Sun, Y.; Chen, Y.; Li, Z.; Zhu, H.; Zhang, G.; Tang, D. Passively Q-switched multiple visible wavelengths switchable YVO4 Raman laser. *J. Lumin.* **2020**, *228*, 117650. [CrossRef]

16. Duan, Y.M.; Zhu, H.Y.; Huang, C.H.; Zhang, G.; Wei, Y. Potential sodium D2 resonance radiation generated by intra-cavity SHG of a c-cut Nd:YVO4 self-Raman laser. *Opt. Express* **2011**, *19*, 6333–6338. [CrossRef] [PubMed]

17. Taylor, L.; Feng, Y.; Calia, D.B. High power narrowband 589 nm frequency doubled fibre laser source. *Opt. Express* **2009**, *17*, 14687–14693. [CrossRef]

18. Ledentsov, N.N.; Shchukin, V.A.; Shernyakov, Y.M.; Kulagina, M.M.; Payusov, A.S.; Gordeev, N.Y.; Maximov, M.V.; Zhukov, A.E.; Denneulin, T.; Cherkashin, N. Room-temperature yellow-orange (In,Ga,Al)P-GaP laser diodes grown on (n11) GaAs substrates. *Opt. Express* **2018**, *26*, 13985–13994. [CrossRef] [PubMed]

19. Leinonen, T.; Korpijärvi, V.-M.; Härkönen, A.; Guina, M. 7.4W yellow GaInNAs-based semiconductor disk laser. *Electron. Lett.* **2011**, *47*, 1139–1140. [CrossRef]

20. Lee, A.J.; Spence, D.J.; Piper, J.A.; Pask, H.M. A wavelength-versatile, continuous-wave, self-Raman solid-state laser operating in the visible. *Opt. Express* **2010**, *18*, 20013–20018. [CrossRef] [PubMed]

21. Chen, Y.F.; Pan, Y.Y.; Liu, Y.C.; Cheng, H.P.; Tsou, C.H.; Liang, H.C. Efficient high-power continuous-wave lasers at green-lime-yellow wavelengths by using a Nd:YVO4 self-Raman crystal. *Opt. Express* **2019**, *27*, 2029–2035. [CrossRef]

22. Chen, Y.F.; Li, D.; Lee, Y.M.; Lee, C.C.; Huang, H.Y.; Tsou, C.H.; Liang, H.C. Highly efficient solid-state Raman yellow-orange lasers created by enhancing the cavity reflectivity. *Opt. Lett.* **2021**, *46*, 797–800. [CrossRef] [PubMed]

23. Chen, J.C.; Ho, Y.W.; Tu, Y.C.; Liang, H.C.; Chen, Y.F. High-Peak-Power Passively Q-Switched Laser at 589 nm with Intracavity Stimulated Raman Scattering. *Crystals* **2023**, *13*, 334. [CrossRef]

24. Chen, Y.F.; Chen, K.Y.; Liu, Y.C.; Chen, C.M.; Tsou, C.H.; Liang, H.C. Criterion for optimizing high-power acousto-optically Q-switched self-Raman yellow lasers with repetition rates up to 500 kHz. *Opt. Lett.* **2020**, *45*, 1922–1925. [CrossRef] [PubMed]

25. Zayhowski, J. Q-switched operation of microchip lasers. *Opt. Lett.* **1991**, *16*, 575–577. [CrossRef]

26. Zayhowski, J.; Dill, C. Diode-pumped passively Q-switched picosecond microchip lasers. *Opt. Lett.* **1994**, *19*, 1427–1429. [CrossRef]

27. Negri, J.R.; Pirzio, F.; Agnesi, A. Jitter investigation of narrow-bandwidth passively Q-switched Nd:YAG unidirectional ring laser. *Opt. Lett.* **2019**, *44*, 3094–3097. [CrossRef]

28. Pavel, N.; Tsunekane, M.; Taira, T. Composite, all-ceramics, high-peak power Nd:YAG/Cr^{4+}:YAG monolithic micro-laser with multiple-beam output for engine ignition. *Opt. Express* **2011**, *19*, 9378–9384. [CrossRef]

29. Chen, Y.F.; Chien, P.Y.; Lee, C.C.; Huang, K.F.; Liang, H.C. Timing jitter reduction of passively Q-switched solid-state lasers by coupling resonance between pumping and firing rates. *Opt. Lett.* **2020**, *45*, 2902–2905. [CrossRef]

30. Chen, Y.F.; Hsieh, M.X.; Tu, Y.C.; Lee, C.C.; Yu, Y.T.; Tsou, C.H.; Liang, H.C. Pedagogically fast model to evaluate and optimize passively Q-switched Nd-doped solid-state lasers. *Opt. Lett.* **2021**, *46*, 1588–1591. [CrossRef]

31. Chen, C.; Wu, Y.; Jiang, A.; Wu, B.; You, G.; Li, R.; Lin, S. New nonlinear-optical crystal: LiB$_3$O$_5$. *J. Opt. Soc. Am. B* **1989**, *6*, 616–621. [CrossRef]

32. Chen, J.Y.; Sua, Y.M.; Fan, H.; Huang, Y.P. Modal phase matched lithium niobate nanocircuits for integrated nonlinear photonics. *OSA Continuum* **2018**, *1*, 229–242. [CrossRef]

33. Jia, Y.; Wang, L.; Chen, F. Ion-cut lithium niobate on insulator technology: Recent advances and perspectives. *Appl. Phys. Rev.* **2021**, *8*, 011307. [CrossRef]
34. Zhao, S.; Huang, C.; Zhang, H. Crystal growth and properties of lithium triborate. *J. Cryst. Growth* **1990**, *99*, 805–810.
35. Aparajit, C.; Jana, K.; Lad, A.D.; Ved, Y.M.; Couairon, A.; Ravindra Kumar, G. Efficient second-harmonic generation of a high-energy, femtosecond laser pulse in a lithium triborate crystal. *Opt. Lett.* **2021**, *46*, 3540–3543. [CrossRef]
36. Nikogosyan, D.N. *Nonlinear Optical Crystals: A Complete Survey*; Springer: Berlin/Heidelberg, Germany, 2005.
37. Velsko, S.P.; Webb, M.; Davis, L.; Huang, C. Phase matched harmonic generation in lithium triborate (LBO). *IEEE J. Quantum Electron.* **1991**, *27*, 2182–2192. [CrossRef]
38. Tang, Y.; Cui, Y.; Dunn, M.H. Thermal dependence of the principal refractive indices of lithium triborate. *J. Opt. Soc. Am. B* **1995**, *12*, 638–643. [CrossRef]